AIAA AVIATION Forum
12-16 June 2023, San Diego, CA and Online
AIAA AVIATION 2023 Forum

10.2514/6.2023-3243

Wall-Modeled Large-Eddy Simulation of Supersonic Flow over Backward-Facing Step for Aero-Optical Distortion Analysis

Pedro Castillo* and Andreas Gross†

New Mexico State University, Las Cruces, NM 88003

Aaron Fassler‡, Sergey Leonov§ and Stanislav Gordeyev¶

Notre Dame University, Notre Dame, IN 46556

This paper reports on compressible wall-modeled large-eddy simulations of a Mach two turbulent boundary layer flow over a cavity. The cavity is defined by a backward-facing step and a compression ramp. The freestream and wall boundary conditions as well as the momentum thickness Reynolds number for the simulations are identical to those of experiments in the Tri-Sonic Wind Tunnel at Notre Dame University. The objective of the research is to understand and predict the aero-optical distortion caused by high-speed turbulent boundary layer flows over optical windows with film cooling. For the present simulation, the cooling film was not considered. Profiles of the root-mean-square velocity fluctuations upstream of the step and velocity profiles downstream of the step compare favorably with available data in the literature. The normalized root-mean-square optical path distortion for the approach boundary layer is in good agreement with a semi-analytical model by Notre Dame University. A preliminary analysis of the optical path distortion downstream of the step indicates a large streamwise variation for the recirculation region and moderate fluctuations downstream of reattachment.

I. Introduction

Flight vehicles rely on optical sensors for tasks such as target acquisition and tracking as well as landmark-based navigation. Such sensors are placed behind optical windows. Other applications, such as directed energy and optical communication, also require windows. At high flight Mach numbers, considerable aero-thermodynamic heating necessitates active cooling of optical windows. Film cooling, which sees widespread application in turbomachinery, is an attractive candidate for the cooling of optical windows. A backward facing step is required to introduce the cooling film gas. The cooling film static pressure is ideally matched to the outside pressure to avoid compression and expansion waves and keep the shear layer parallel to the wall. The cooling film gas does not necessarily need to have the same chemical composition as the atmosphere. This introduces challenges for the optical system: The density and velocity of the cooling film will affect the streamwise growth of the layer over the optical window. As seen in van Dyke's album of fluid motion,[1] strong density and velocity gradients can lead to pronounced spanwise coherent flow structures in turbulent shear layers. Large density gradients associated with the turbulent flow structures as well as the mixing of dissimilar gases with different refraction indices can lead to large aero-optical distortions. The understanding of the source of the aero-optical distortions and the development of models for predicting

*Graduate Research Assistant, Mechanical and Aerospace Engineering Department. AIAA Member.
†Associate Professor, Mechanical and Aerospace Engineering Department. AIAA Associate Fellow.
‡Graduate Research Assistant, Aerospace and Mechanical Engineering Department. AIAA Member.
§Research Professor, Aerospace and Mechanical Engineering Department. AIAA Associate Fellow.
¶Associate Professor, Aerospace and Mechanical Engineering Department. AIAA Associate Fellow.

their intensity (similar to the Notre Dame model for boundary layer flows by Gordeyev et al.[2]) are the main objectives of this research.

A multi-tiered approach of experiments and theory at Notre Dame University (ND) as well as wall-modeled large-eddy simulations (WMLES) at New Mexico State University (NMSU) is taken to understand and model the aero-optics of turbulent supersonic boundary layer flows over optical windows with film cooling. The experiments are carried out in the Tri-Sonic Wind Tunnel at ND. First experiments focused on Mach 2 flow over the cavity without film cooling. Without film cooling, the flow resembles the flow over a cavity that is defined by a backward-facing step and a compression ramp. For the chosen approach boundary layer and freestream conditions as well as geometry, the boundary layer reattaches far upstream of the compression ramp.

Numerous experimental (e.g. Refs. 3–6) and numerical (e.g. Refs. 7–10) studies have been conducted to understand the flow physics of subsonic and supersonic flows past geometric discontinuities that are characterized by a sudden change of the surface slope. Charwat et al.[7] considered laminar and turbulent separation from an isolated backward-facing step of height h. Reattachment was $7h$ downstream of the step for a laminar boundary layer and $5h$ downstream of the step for a turbulent boundary layer. Experiments and simulations by Liu et al.[10] showed that the reattachment length decreases with increasing inflow Mach number. Rom and Seginer[3] considered a laminar supersonic boundary layer flow over a backward-facing step. The wall heat-transfer was found to depend on the ratio of the boundary layer thickness to the step height and to decrease downstream from the step.

When collimated light is propagated through compressible turbulent boundary and shear layers, aero-optical effects such as image blurring, beam jitter, and offsetting occur. The density fluctuations associated with supersonic turbulent shear layer flows over optical window cavities are the primary cause for optical aberrations.[11,12] According to Yi et al.[13] and Zhi et al.,[14] coherent flow structures cause strong aero-optical distortions, especially in the reattachment region. Ayyalasomayajula et al.[15] found that wavefront phase aberrations and root-mean-square optical path differences (OPD_{rms}) mainly result from shocklets downstream of the backward facing step.

The present paper reports on a WMLES of the Mach 2 flow over the cavity geometry of the Notre Dame experiments without film cooling. Using analytical functions, a computational grid for the cavity simulation was generated. The computational grid consists of two blocks, one for the approach boundary layer (BL) and one for the backward facing step, cavity, and compression ramp. The approach boundary layer momentum-thickness Reynolds number of the experiment, $Re_\theta = 21,750$, is matched in the simulation. First, the approach boundary layer simulation is validated by comparison with available data in the literature. The normalized OPD_{rms} for the approach boundary layer is in good agreement with predictions by the Notre Dame model.[2] Then, the cavity flow is analyzed in detail. Finally, the OPD of the cavity flow is computed for various streamwise intervals downstream of the backward facing step.

II. Methodology

A. Numerical Method

The compressible Navier-Stokes equations in the finite volume formulation were solved with a research computational fluid dynamics code.[16,17] The convective fluxes were computed with the Lax-Friedrichs (maximum eigenvalue over stencil width) scheme and interpolated onto the cell faces with a ninth-order-accurate weighted essentially non-oscillatory scheme.[18] A fourth-order-accurate discretization was employed for the viscous terms. The governing equations were integrated in time with the second-order-accurate implicit trapezoidal rule. The perfect gas state equation was used to model the gas behavior. The dynamic viscosity was obtained from Sutherland's law.

B. Reference Parameters and Non-Dimensionalization

The freestream Mach number for the Tri-Sonic Wind Tunnel (TWT) experiments at ND is $M_\infty = 2$. The operating gas is air. The stagnation pressure is $p_0^* = 100psi = 689.5kPa$ and the stagnation temperature is $T_0^* = 300K$. Here, the asterisk indicates dimensional quantities. The unit Reynolds number is $Re_{1m} = 79.2 \times 10^6\, 1/m$. Based on schlieren flow visualisations, the boundary layer thickness was estimated as $\delta^* = 3.2mm$. Using equations from Smits and Dussage,[19] the momentum thickness is approximately $\theta^* = 0.275mm$ and the momentum thickness Reynolds number is $Re_\theta = Re_{1m} \times \theta^* = 21,750$.

All length scales were made dimensionless with an arbitrary reference length, $L^*_{ref} = 0.10854m$. The freestream velocity, $u^*_\infty = 517.75m/s$, was taken as reference velocity. Density was made dimensionless by the freestream density, $\rho^*_\infty = 1.8409kg/m^3$. The temperature and pressure were made dimensionless with the freestream temperature, $T^*_\infty = 166.7K$, and two times the freestream dynamic pressure, $\rho^*_\infty u^{*2}_\infty$, respectively. Time was normalized by L^*_{ref}/u^*_∞. The dynamic viscosity was made dimensionless with the freestream viscosity, $\mu^*_\infty = 0.11325 \times 10^{-04} kg/(ms)$. The Reynolds number based on the reference quantities is $Re = 9.135 \times 10^6$. The laminar and turbulent Prandtl number were 0.71 and 0.9, respectively. The computational timestep was $\Delta t = 0.0005$.

C. Wall-Modeling

For simulations of high-Reynolds number turbulent wall-bounded flows, the near-wall grid resolution requirement can become prohibitive unless the near-wall turbulence is modeled. For compressible flows, wall models are required for both the momentum and energy equation. For the derivation of the wall model, the wall-normal pressure gradient is assumed to be zero, $\partial P/\partial y = 0$, which is a valid assumption for zero-pressure gradient flat plate boundary layer flows. In addition, the parallel flow assumption is invoked. With these assumptions, the filtered momentum and energy equations simplify to[20]

$$\frac{\partial}{\partial y}\left[\frac{1}{Re}(\mu+\mu_T)\frac{\partial u}{\partial y}\right] = 0, \tag{1}$$

$$\frac{\partial}{\partial y}\left[\frac{1}{Re}(\mu+\mu_T)u\frac{\partial u}{\partial y} + \frac{1}{(\gamma-1)M^2_\infty}\frac{1}{Re}\left(\frac{\mu}{Pr}+\frac{\mu_T}{Pr_T}\right)\frac{\partial T}{\partial y}\right] = 0. \tag{2}$$

The preceding wall model equations are solved numerically from the wall, $y = 0$, to a point, $y = y_p$, where the wall model velocity and temperature are matched to their respective resolved quantities (i.e., the matching point). The boundary conditions are $u(0) = 0$ & $T(0) = T_w$ at the isothermal wall and $u(y_p) = u_p$ & $T(y_p) = T_p$ at the matching point.

The wall-model equations (Eqs. 1 and 2) were solved with a shooting method with first-order-accurate wall-normal integration. For the present results, the matching point was set to the third cell off the wall. For the integration, the distance from the wall to the matching point, y_p, was sub-divided by one thousand intervals, Δy. This was found to yield converged wall-model solutions. A Newton-Raphson iteration was employed for finding the velocity and temperature gradient at the wall,

$$\begin{bmatrix} u_p\left(\frac{\partial u}{\partial y}\big|_w, \frac{\partial T}{\partial y}\big|_w\right) \\ T_p\left(\frac{\partial u}{\partial y}\big|_w, \frac{\partial T}{\partial y}\big|_w\right) \end{bmatrix} + \begin{bmatrix} \partial u_p/\frac{\partial u}{\partial y}\big|_w & \partial u_p/\frac{\partial T}{\partial y}\big|_w \\ \partial T_p/\frac{\partial u}{\partial y}\big|_w & \partial T_p/\frac{\partial T}{\partial y}\big|_w \end{bmatrix} \begin{bmatrix} \Delta\frac{\partial u}{\partial y}\big|_w \\ \Delta\frac{\partial T}{\partial y}\big|_w \end{bmatrix} = \begin{bmatrix} u_p \\ T_p \end{bmatrix}. \tag{3}$$

The wall-model equations not only provide the near-wall velocity and temperature profile, but also the wall velocity shear, $\partial u/\partial y(0)$, and temperature gradient, $\partial T/\partial y(0)$. In more compact form, Eqn. 3 can be expressed as

$$\mathbf{y}_p\left(\mathbf{x}_p\right) + \mathbf{A}\,\Delta\mathbf{x}_p = \mathbf{y}_p, \tag{4}$$

where the gradients in matrix $\mathbf{A}$ are evaluated numerically. The velocity and temperature gradients at the wall are updated according to

$$\Delta\mathbf{x}_p = \mathbf{A}^{-1}\left[\mathbf{y}_p - \mathbf{y}_p\left(\mathbf{x}_p\right)\right] \tag{5}$$

$$\mathbf{x}_p \Leftarrow \mathbf{x}_p + \Delta\mathbf{x}_p. \tag{6}$$

The convergence criterion for the present results was $\left|\mathbf{y}_p - \mathbf{y}_p\left(\mathbf{x}_p\right)\right| < 10^{-6}$.

D. Sub-Grid Stress and Heat Flux

The sub-grid stress (SGS) tensor, $\bar{\rho}\tau_{ij} = \bar{\rho}\overline{u'_i}\,\overline{u'_j} - \overline{\rho u'_i u'_j}$, is modeled as

$$\bar{\rho}\tau_{ij} = 2\mu_T\left(S_{ij} - \frac{1}{3}S_{kk}\delta_{ij}\right) - \frac{2}{3}\bar{\rho}k\delta_{ij}\,, \tag{7}$$

with sub-grid eddy-viscosity, μ_T, strain rate tensor, S_{ij}, Kronecker symbol, δ_{ij}, and turbulence kinetic energy, k. The sub-grid heat flux is modeled as

$$q_i = -c_p \frac{\mu_T}{Pr_T} \frac{\partial T}{\partial x_i}\,, \tag{8}$$

with specific heat, $c_p = 1/[(\gamma - 1)\, M_\infty^2]$.

E. Sub-Grid Stress Model

The WALE model by Nicoud and Ducros[21] was employed for computing the sub-grid (unresolved) eddy-viscosity,

$$\mu_T = \bar{\rho}(C_w \Delta)^2 \frac{(S_{ij}^d S_{ij}^d)^{3/2}}{(S_{ij} S_{ij})^{5/2} + (S_{ij}^d S_{ij}^d)^{5/4}}\,, \tag{9}$$

where

$$S_{ij}^d = \frac{1}{2}\left(g_{ij}^2 + g_{ji}^2\right) - \frac{1}{3}\delta_{ij} g_{kk}^2 \tag{10}$$

is the trace-less symmetric part of the square of the velocity gradient tensor and $g_{ij}^2 = g_{ik} g_{kj}$. For the present results, the model constant, C_w, was taken as 0.325. The grid length-scale, Δ, was taken as the geometric average of the cell dimensions. The isentropic unresolved TKE was computed as

$$k = \frac{1}{2}\tau_{kk} = \left(\frac{\mu_T}{0.094 Re \rho \Delta}\right)^2 . \tag{11}$$

F. Computational Grid

Using analytical functions, a body-fitted computational grid was generated for the geometry of the ND experiments (Fig. 1). The grid is divided into two sub-domains or blocks. Block 1 is rectangular and features a constant grid-line spacing in the streamwise and spanwise directions. Near the outflow, the streamwise grid-line spacing is reduced to resolve the corner flow. A wall-normal grid line spacing of $\Delta y/\delta = 0.02$ was employed between the wall and $y/\delta = 0.2$. Outside the near-wall region ($y/\delta \leq 0.2$), the wall-normal grid line stretching is initially 5% and then decreases away from the wall. Block 2 is close to rectangular and features a compression ramp at the outflow. The height of the backward facing step is $h = 0.04605$. The compression ramp starts at $x = 2.2121$ downstream of the backward facing step. The compression ramp angle is $\alpha = 4deg$. The streamwise grid line spacing is reduced at the block 2 inflow to resolve the rear side of the backward facing step. Downstream of the block 2 inflow, the streamwise grid line spacing is first constant and then increases near the outflow to dissipate flow structures before they leave the computational domain. Downstream of the block 2 inflow, the grid lines are redistributed in the wall-normal direction to obtain a more balanced grid line distribution. Similar to block 1, a layer with constant wall-normal grid distribution is employed at the wall. For both blocks 1 and 2, the grid line distribution in the spanwise direction is equidistant. The spanwise grid extent is 0.12 and the number of cells in the spanwise direction is 160. Table 1 provides an overview of some of the pertinent grid properties.

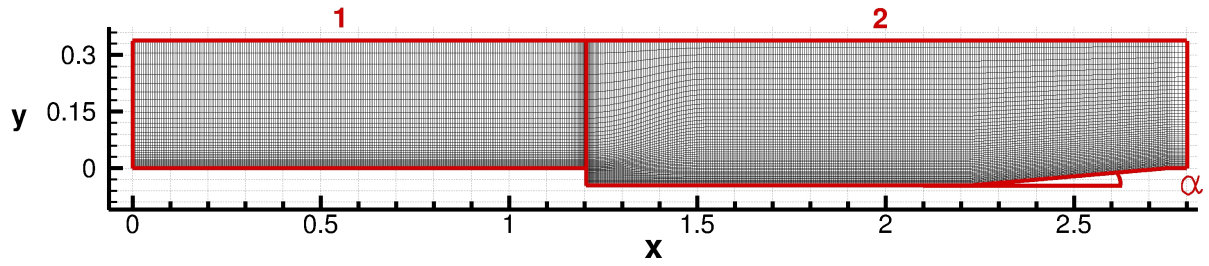

Figure 1. Computational grid (every other grid line is omitted).

Table 1. grid properties.

Block	Domain size		Number of cells	Total number of cells
1 (Approach BL)	$1.2044 \times 0.3380 \times 0.12$	$26.4h \times 7.4h \times 2.6h$	$512 \times 64 \times 160$	5.24×10^6
2 (Cavity)	$1.5965 \times 0.3841 \times 0.12$	$35h \times 8.4h \times 2.6h$	$666 \times 102 \times 160$	10.86×10^6

G. Boundary Conditions

No-slip and no-penetration conditions were enforced at the wall. The wall was considered to be adiabatic as the run time of the experiments is several seconds. Flow periodicity was enforced in the spanwise direction. Dirichlet conditions were applied at the inflow and freestream boundary, and Newman conditions were employed at the outflow boundary.

The rescaling and recycling method by Stolz and Adams[22] was employed to sustain a turbulent approach boundary layer flow. For the present simulations, the recycling plane was placed at $x = 1$. More details about the implementation of the rescaling and reycling method can be found in Gross et al.[23] The rescaling and recycling method can lead to an accumulation of disturbances in the freestream unless some damping is applied. Therefore, between the boundary layer edge, y_e, and freestream boundary, y_∞, the density and temperature were forced to their respective freestream values via continuity and energy equation right-hand-side terms,

$$\frac{\partial \rho}{\partial t} + \nabla \cdot (\rho \mathbf{u}) = C(1-\rho), \tag{12}$$

$$\frac{\partial (\rho E)}{\partial t} + \nabla \cdot (\rho E \mathbf{u}) = C\rho c_v (1-T), \tag{13}$$

with $c_v = 1/[\gamma(\gamma-1)\,M^2]$ and $C = (y - y_e)/(y_\infty - y_e)$. Inevitably, the forcing terms also damp acoustic waves that are radiated by the boundary layer and shear layer.

H. Optical Path Length and Optical Path Difference

To investigate the optical aberrations, the density fields were first converted into index-of-refraction, n, fields via the linear Gladstone-Dale relation,[24]

$$n = 1 + K_{GD}\rho\,, \tag{14}$$

where $K_{GD} = 2.27 \times 10^4\, m^3/kg$ is the Gladstone-Dale constant for air over the pressure and temperature range of the present simulations.[25,26] Wall-normal integration of the index-of-refraction from the wall to the freestream provides the optical path length,

$$OPL(x,z,t) = \int_0^y n(x,y,z,t)dy\,. \tag{15}$$

The mean piston, tip, and tilt is then removed from the OPL to obtain the optical path difference,

$$OPD(x,z,t) = OPL(x,z,t) - (m_x x + m_z z + b)\,. \tag{16}$$

This correction accounts for the boundary layer growth. Following Wang and Wang,[27] at each time instant the coefficients for the correction are found by minimizing,

$$R = \int_x \int_z \left[OPL(x,z,t) - (m_x x + m_z z + b)\right]^2 dxdz\,, \tag{17}$$

over an aperture. Aperture in this context refers to the x and z range over which the OPD is computed. The minimization of Eqn. 17 provides a system of equations that is solved for the unknowns m_x, m_z and b.

In the study of aero-optical properties of turbulent boundary layers, the root-mean-square of the OPD is often considered,

$$OPD_{rms} = \sqrt{\overline{\langle OPD^2(x,z,t)\rangle}}\,. \tag{18}$$

In this paper, the OPD_{rms} obtained from the present simulations is compared with a relationship proposed by Gordeyev et al.[2] (Notre Dame model),

$$f\left(M_\infty\right) = \frac{OPD_{rms}}{K_{GD}\rho_\infty c_f^{0.5} M_\infty^2 \delta} \,. \tag{19}$$

III. Approach Boundary Layer

The approach boundary layer simulation was advanced in time until the flow became statistically stationary. Then a time-average and statistical quantities were computed over a time-interval of $t_{avg/stat} = 10$. The time-average and statistics were averaged in the homogeneous spanwise direction. The compressible displacement thickness, δ^*, momentum thickness, θ, and incompressible shape factor, H_i, are plotted in Fig. 2a. The incompressible shape factor asymptotically approaches a value of 1.3, which is inside the commonly accepted range for turbulent boundary layers ($1.3 < H_i < 1.4$).

In Fig. 2b, the van Driest transformed velocity profile,

$$u^{VD} = \int \sqrt{\frac{\rho}{\rho_w}} du^+ \,, \tag{20}$$

for $x = 1.1$ is plotted. The red dashed line represents the modeled part of the WMLES profile and the solid red line represents the resolved part of the profile. The matching point (for the wall model) is at $y^+ \approx 390$ and well within the log-layer. The profile obtained from the WMLES is in good agreement with relationships for the viscous sublayer, $u^+ = y^+$, (dotted black line) and the log-layer, $u^+ = 5 + \ln(y^+)/0.41$ (dashed black line).

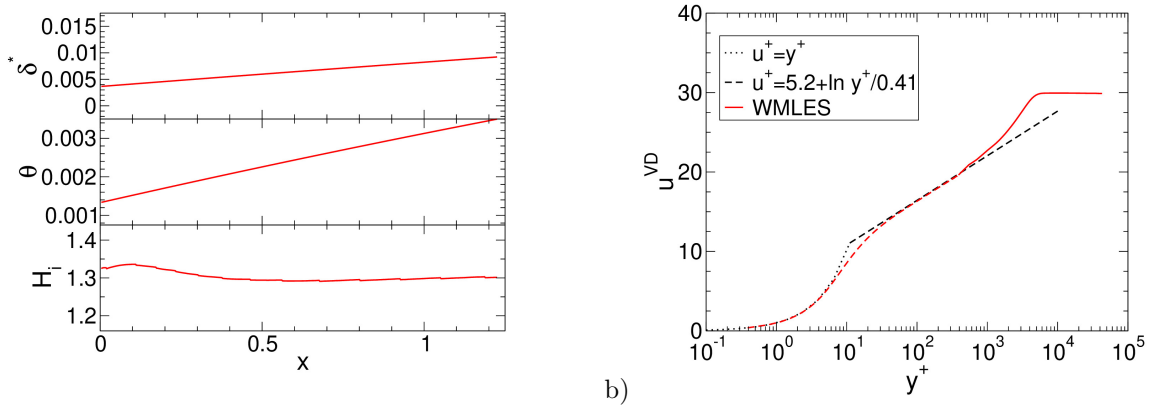

Figure 2. a) Compressible displacement and momentum thickness, and incompressible shape factor. b) Velocity profile in wall units for $x = 1.1$.

The size of the computational domain in the streamwise, wall-normal, and spanwise direction is $31\delta_{x=1.1} \times 9\delta_{x=1.1} \times 3\delta_{x=1.1}$, where $\delta_{x=1.1} = 0.037$ is the boundary layer thickness at $x = 1.1$. Two-point correlations of the density fluctuations were computed in the streamwise and spanwise directions (Fig. 3) for two wall-normal locations, the wall-model matching point (black line) and the boundary layer edge at $x = 1.1$ (red line). The streamwise correlation for the matching point exhibits a peak at $27\delta_{x=1.1}$, which is the location of the recycling plane. Decorrelation of the fluctuations is achieved over one to two boundary layer thicknesses in both directions and for both wall-normal locations. This indicates that the streamwise and spanwise extent of the computational domain are sufficient for turbulent boundary layer simulations.[22]

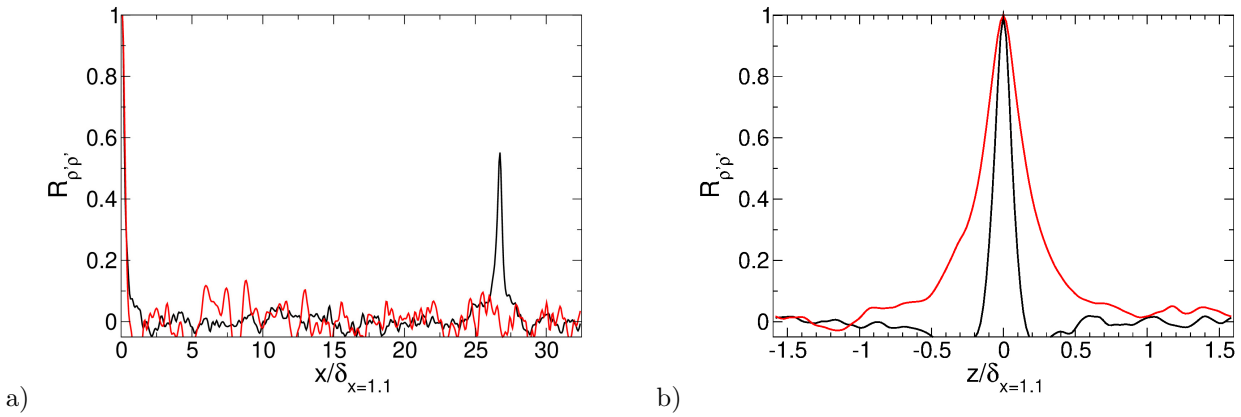

Figure 3. Two-point density correlations in the a) streamwise and b) spanwise direction.

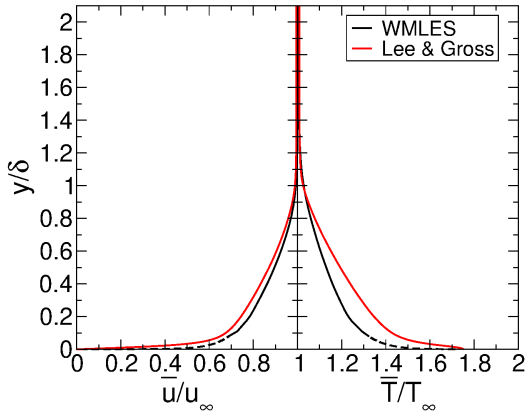

Figure 4. Velocity and temperature profiles (---, from wall model, ——, resolved).

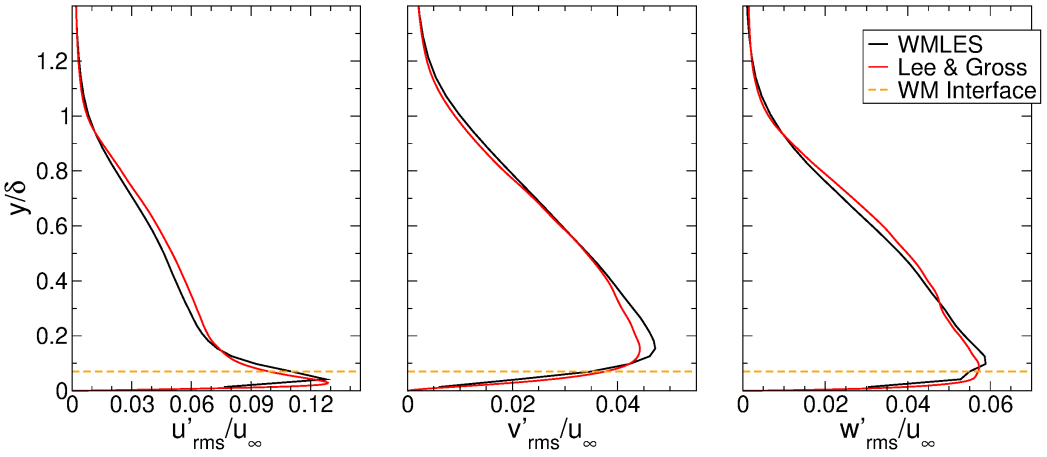

Figure 5. Profiles of resolved root-mean-square velocity fluctuations.

Velocity and temperature profiles for $x = 1.1$ are plotted in Fig. 4. As before, the dashed part of the profiles is modeled and the solid part is resolved. For comparison, profiles from a wall-resolved LES (WRLES) by Lee and Gross[28] of a $M_\infty = 2.05$ turbulent boundary layer over an adiabatic flat plate at a roughly 10 times lower momentum thickness Reynolds number are included. Good agreement between the WMLES and WRLES velocity profiles is observed. Concerning the temperature profiles, the adiabatic wall temperature is lower for the WMLES.

The root-mean-square (RMS) velocity fluctuations in the streamwise, wall-normal and spanwise direction, normalized by the freestream velocity, are compared in Fig. 5. The dashed orange lines indicate the wall model matching point. Below the matching point, the RMS fluctuations obtained from the WRLES are ill-defined. Good agreement is observed between the RMS fluctuations obtained from the present WMLES and the earlier WRLES by Lee & Gross.[28]

IV. Cavity Flow

The approach boundary layer flow was passed into the cavity flow domain (block 2). The cavity flow simulation was advanced in time until the flow became statistically stationary. Then a time-average and statistical quantities were computed over a time-interval of $t_{avg/stat} = 8$. The time average and statistics were averaged in the homogeneous spanwise direction.

Two-point density correlations in the spanwise direction for two streamwise locations, $x_1 = 1.609$ and $x_2 = 2.185$, are presented in Fig. 6. Correlations were computed for the wall-normal location of the matching point, $y/h = 0.052$, and the boundary layer edge (for $x_1 = 1.609$ and $x_2 = 2.185$). The solid black line is for x_1 and the dashed black line is for x_2. The solid blue line is for x_1 and the solid red line is for x_2. The boundary layer thickness is $\delta = 0.047$ at x_1 and $\delta = 0.06$ at x_2. At the wall-model interface location (black dashed line and black solid line), the density fluctuations decorrelate at one boundary layer thickness for both x-locations. At the boundary layer edge (blue and red solid lines), decorrelation of the fluctuations is achieved over roughly two boundary layer thicknesses. This indicates that the spanwise extent of the computational domain is sufficient.[22]

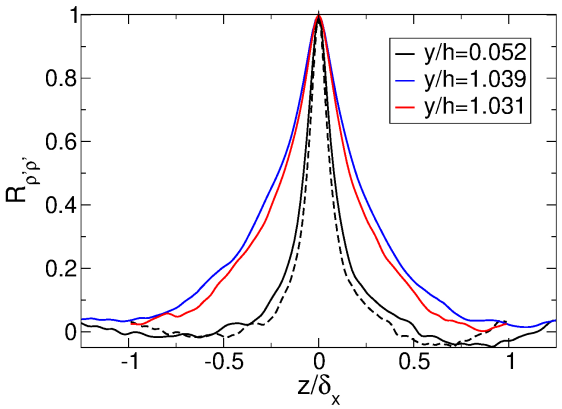

Figure 6. Two-point density correlations in the spanwise direction for $x_1 = 1.609$ (solid black line and blue line) and $x_2 = 2.185$ (dashed black line and solid red line).

Instantaneous iso-contours of the density gradient magnitude at $z = 0.06$ are shown in Fig. 7. Such images are referred to as "numerical Schlieren" images. Different from experimental Schlieren images, the density gradients are not integrated in the spanwise direction. For comparison, a recent Schlieren image from the Notre Dame University experiments is provided in Fig. 8. The Schlieren images reveal a Prandtl-Meyer expansion fan that emanates from the top corner of the backward facing step. The expansion fan is associated with the downward flow turning of the separated boundary layer immediately downstream of the step and an associated flow expansion. The separated boundary layer (or shear layer) encloses a recirculation region at the base of the step. The flow turning angle between the shear layer and the wall of the test section is approximately $15.5deg$. The flow is then turned back in a direction parallel to the test section wall.

This turning is associated with compression waves in the reattachment region that coalesce into an oblique shockwave with a shock angle of $19.5deg$. Both angles are in agreement with previously published data by Hartfield et al.[4] and McDaniel et al.[29] Another oblique shockwave originates from the compression corner near the outflow.

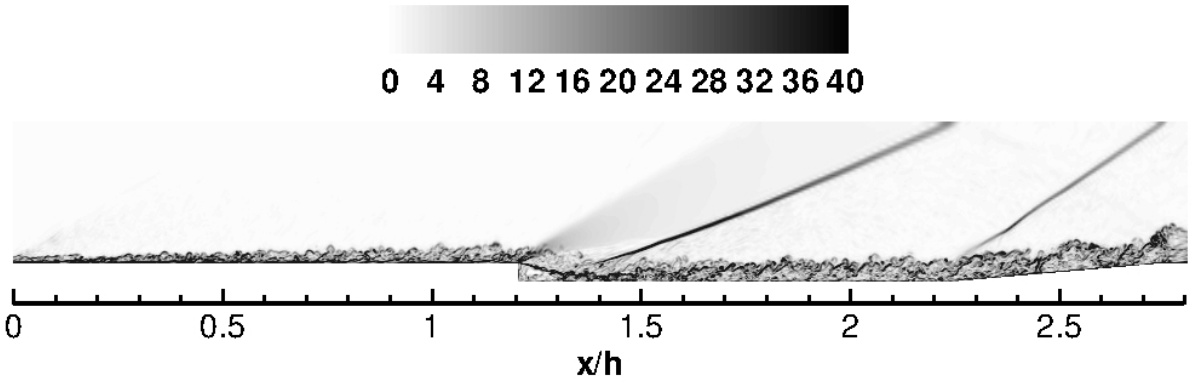

Figure 7. Instantaneous iso-contours of density gradient magnitude at $z = 0.06$.

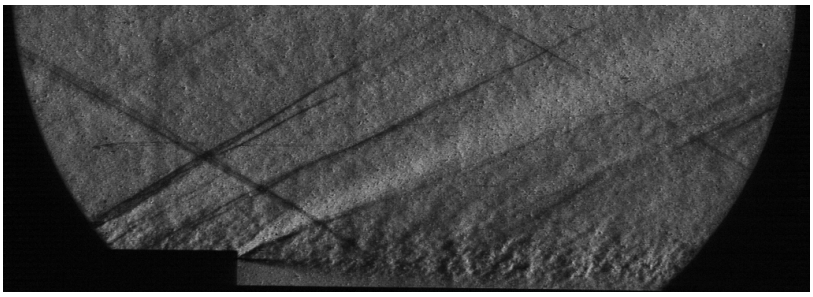

Figure 8. Schlieren visualization from Notre Dame University experiments.

Mean flow visualizations are provided in Fig. 9. All distances are normalized by the step height, h. Contours of the streamwise velocity and streamlines are shown in Fig. 9a. The streamlines turn gradually across the expansion fan and abruptly when passing through the oblique shockwaves. The flow recirculates in the separated flow region behind the step. The pressure is essentially uniform across the attached boundary layers and the recirculation region (Fig. 9b). The pressure contour lines inside the expansion fan are straight and represent the expansion waves. The forward edge of the expansion fan has an angle of 30 deg, which matches the Mach angle, $\mu = \text{asin}M_\infty^{-1} = 30deg$. The foot of both oblique shockwaves is formed by coalescing compression waves. As the flow passes through the oblique shockwaves, the pressure increases abruptly. Iso-contours of the turbulence kinetic energy, TKE, are illustrated in Fig. 9c. The shear layer over the separated flow region is a region of strong turbulence production. A local maximum of the TKE is observed at reattachment. Downstream of reattachment, as the turbulent boundary layer relaxes towards equilibrium, the TKE is attenuated.[10]

For backward-facing step flows, the reattachment length, defined as the streamwise distance between the step and the reattachment line, is of interest. In Fig. 10a, the skin-friction coefficient, c_f, is plotted against the streamwise coordinate. The flow separates at the corner and reattaches (in the mean) at x_r (dashed red line marked "'x_r"). As a result of a small secondary separation, the recirculating flow also separates close to the base of the step (dashed red line marked "x_s"). The skin-friction remains very small for the upstream part of the separation bubble ($0 < x/h < 1.5$). Prior to reattachment, the skin-friction increases substantially (with a global minimum at $x/h = 2$). The flow reattaches in the mean at $x/h \approx 2.8$, in good agreement with previously published Mach 2 data by Liu et al.,[10] Bolgar et al.,[30] and Riley et al.[31] The RMS streamwise velocity fluctuations at reattachment are shown in Fig. 10b. For comparison, experimental data by Bolgar et al.[30] are included. Good quantitative agreement is observed between WMLES and experiment.

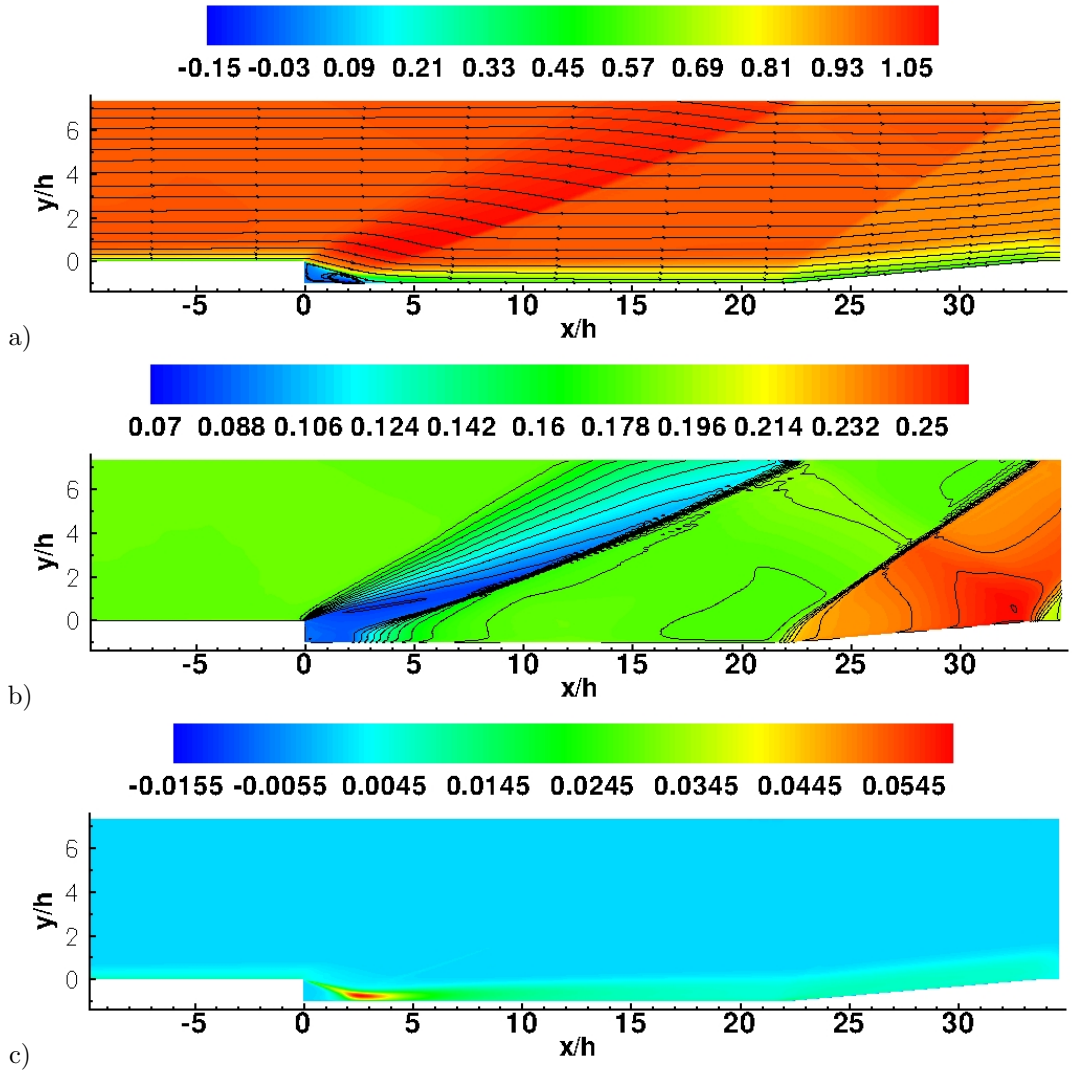

Figure 9. Iso-contours of mean a) streamwise velocity, b) static pressure, and c) turbulent kinetic energy.

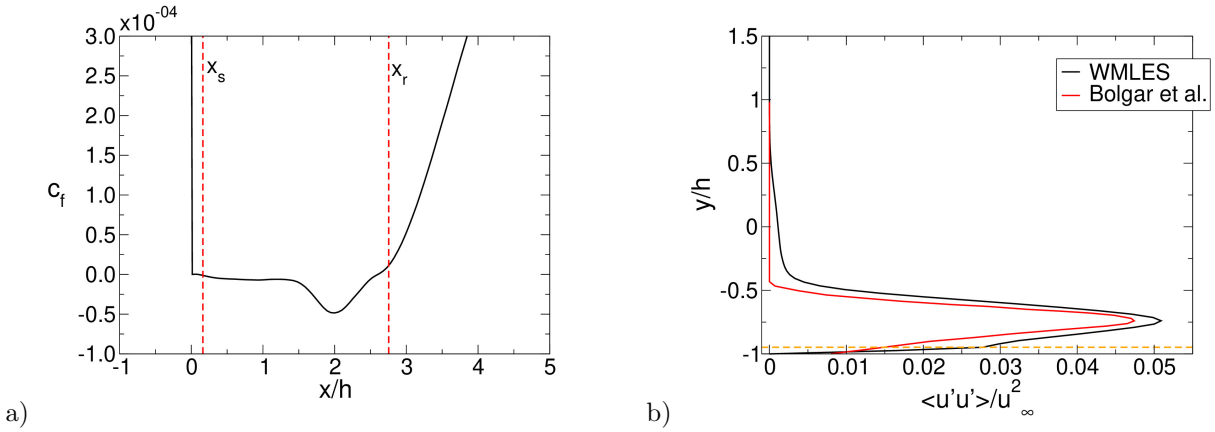

Figure 10. a) Skin-friction coefficient with mean separation and reattachment location. b) Streamwise velocity fluctuations at reattachment.

The streamwise evolution of the velocity profiles upstream of the step, across the recirculation, and downstream of reattachment is illustrated in Fig. 11. Upstream of the step ($x/h < 0$), the velocity profile is typical of turbulent boundary layers. Downstream of the step, at $x/h = 1$, a typical shear layer profile is observed. For $x/h = 2$ and 3, reverse flow is noticed near the wall and the velocity increases across the expansion fan. For $x/h = 3$, experimental[10,29] and numerical[32] results from similar flow fields are included. Particularly good agreement between the present WMLES profile and the experimental data by McDaniel et al.[29] is observed. Downstream of reattachment ($x/h > 3$), for $x/h > 10$ the shape of the velocity profiles gradually recovers that of an equilibrium turbulent boundary layer. For $x/h = 7$, the oblique shockwave reduces the freestream velocity for $y/h < 1$.

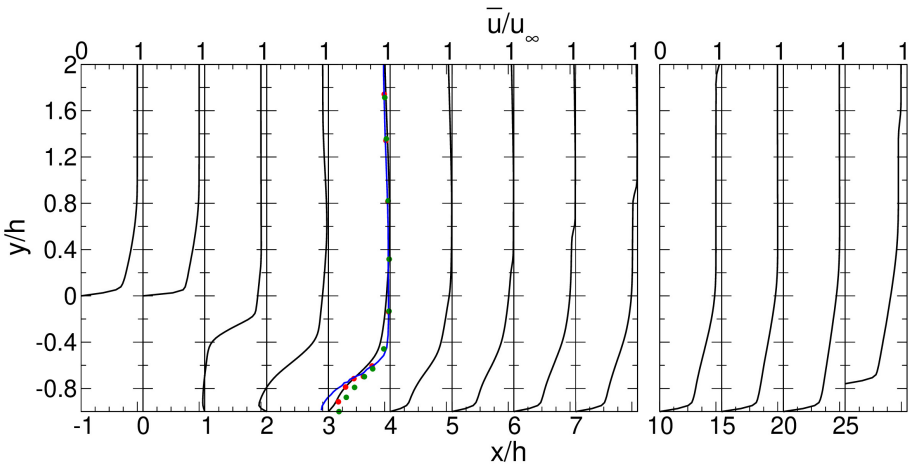

Figure 11. Streamwise evolution of velocity profiles. Experimental data by McDaniel et al.[29] (red dots) and Liu et al.[10] (green dots). Numerical data (blue line) by Soni et al.[32]

V. Aero-Optical Analysis

A total of 2,000 density fields were saved at every five timesteps and the OPD was computed for both the approach boundary layer and the cavity. In Fig. 12, the normalized OPD, $f(M_\infty)$ from Eqn. 19, for the approach boundary layer (block 1) is plotted against the ND model relationship.[33,34] Previously published numerical[35,36] and experimental data[33,34,37] are also included. The $f(M_\infty)$-value from the present WMLES is in good agreement with the reference data. The OPD obtained from the present WMLES deviates 4.5% from the ND model prediction for $M_\infty = 2$.

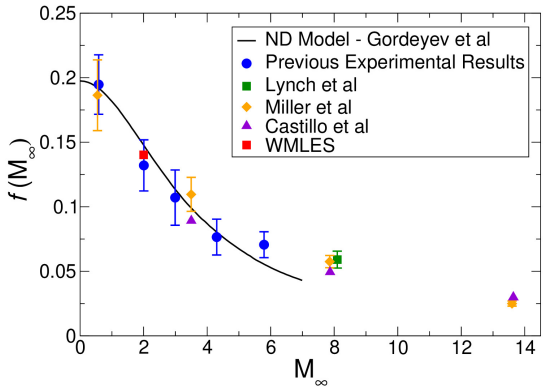

Figure 12. Normalized OPD_{rms}. Notre Dame model,[33,34] numerical[35,36] and experimental data.[38]

For the cavity, four different streamwise intervals were chosen as beam aperture. The four regions are denoted x_1, x_2, x_3, and x_4 in Fig. 13. The streamwise extent of the aperture is nine step heights for x_1 and three strep heights otherwise. For the analysis, the beam incidence angle is normal to the bottom wall. Instantaneous distributions of the OPD for all four apertures are displayed in Figs. 14b-e. For aperture x_1 (Fig. 14a), the OPD follows a sinusoidal behavior and the surface is smooth. This can be explained by the piston, tip and tilt correction (Eq. 16) which is not appropriate for the reattaching turbulent boundary layer. For the locations downstream of reattachment, x_2 through x_4, the OPD exhibits fluctuations across the aperture as would be expected for turbulent boundary layers.

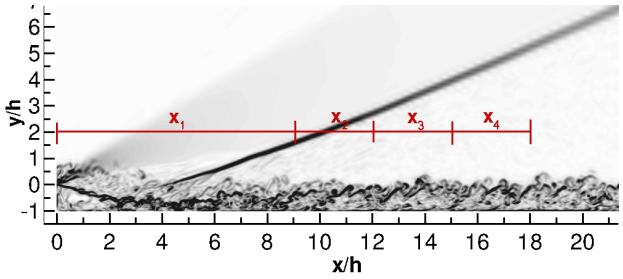

Figure 13. Streamwise intervals for computation of OPD.

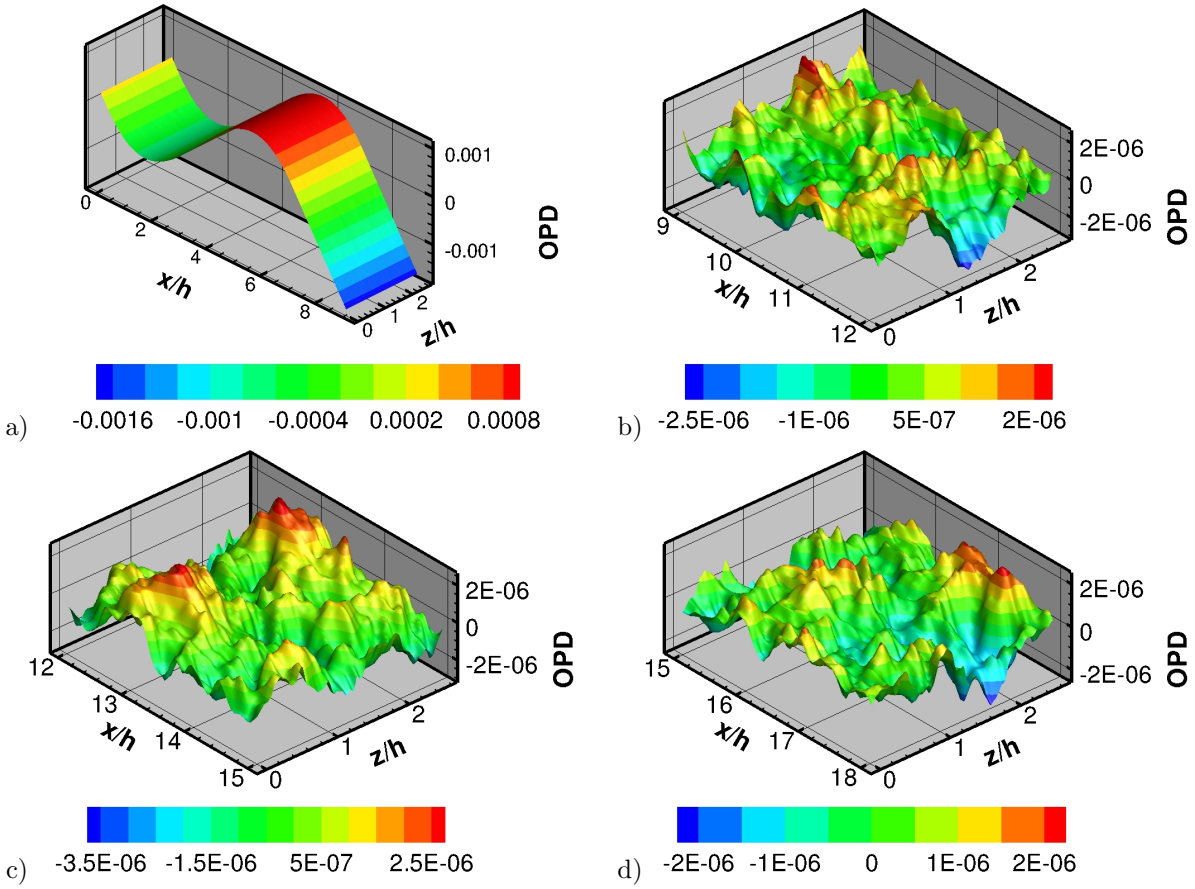

Figure 14. OPD for streamwise intervals a) x_1, b) x_2, c) x_3, and d) x_4.

VI. Conclusions

Cooling films over optical windows in hypersonic flight will cause optical aberrations. Understanding the source of the aberrations and predicting their strength and nature is of interest to the designers of such devices. A multi-tiered approach of experiments and theory at Notre Dame University (ND) and wall-modeled large-eddy simulations (WMLES) at New Mexico State University (NMSU) is taken to understand and model the aero-optics of turbulent supersonic boundary layer flows over optical windows with film cooling. First experiments at ND without film cooling considered Mach 2 flow over a canonical geometry consisting of a backward facing step and a compression ramp. In parallel, a WMLES of the flow was performed at NMSU. The flow field is characterized by a rapid expansion at the backward facing step, a recirculation region at the base of the step, a recompression shock at reattachment, and an oblique shockwave at the compression corner. The reattachment length, mean streamwise velocity profiles, streamwise velocity fluctuations, and shear layer and oblique shock angles, are in good agreement with published numerical and experimental data.

The good accuracy of the present WMLES results motivated and encouraged an analysis of the aero-optical distortions resulting from the density fluctuations in the turbulent boundary layer and the cavity. The RMS optical path distortion (OPD) for the approach boundary layer is in good agrement with a semi-empirical model by Notre Dame University and published experimental data. The OPD downstream of reattachment is representative of turbulent boundary layers and will be analyzed further.

VII. Acknowledgement

This research is funded by the Office of Naval Research (ONR) under grant number N00014-22-1-2454 with Dr. Eric Marineau serving as program manager.

References

[1]Van Dyke, M., *An album of fluid motion*, Vol. 176, Parabolic Press Stanford, 1982.

[2]Gordeyev, S., Jumper, E., and Hayden, T. E., "Aero-Optical Effects on Supersonic Boundary Layers," *AIAA Journal*, Vol. 50, No. 3, 2012.

[3]Rom, J. and Seginer, A., "Laminar Heat Transfer to a Two-Dimensional Backward Facing Step from the High-Enthalpy Supersonic Flow in the Shock Tube," *AIAA Journal*, Vol. 2, 1964, pp. 251–255.

[4]Hartfield Jr., R., Hollo, S., and McDaniel, J., "Planar measurement technique for compressible flows using laser-induced iodine fluorescence," *AIAA Journal*, Vol. 31, No. 3, 1993, pp. 483–490.

[5]Shen, G. and Ma, G., "The Investigation on the Properties and Structures of Starting Vortex Flow Past a Backward-Facing Step by WBIV Technique," *Experiments in Fluids*, Vol. 21, No. 1, 1996, pp. 57–65.

[6]Furuichi, N., Hachiga, T., and Kumada, M., "An Experimental Investigation of a Large-Scale Structure of a Two-Dimensional Backward-Facing Step by Using Advanced Multi-Point LDV," *Experiments in Fluids*, Vol. 36, No. 2, 2004, pp. 274–281.

[7]Charwat, A., Dewey, C., Roos, J., and Hitz, J., "An Investigation of Separated Flows. 1: The Pressure Field," *Journal of Aerospace Sciences*, Vol. 28, 1961, pp. 457–470.

[8]Correa, S. and Warren, R., "Supersonic Sudden-Expansion Flow with Fluid Injection: an Experimental and Computational Study," *AIAA Paper 1989-0389*, 1989.

[9]Yang, A., Hsieh, W., and Kuo, K., "Theoretical Study of Supersonic Flow Separation Over a Rearward-Facing Step," *Journal of Propulsion and Power*, Vol. 13, No. 2, 1997, pp. 324–326.

[10]Liu, H., Wang, B., Guo, Y., Zhang, H., and Lin, W., "Effects of Inflow Mach Number and Step Height on Supersonic Flows over a Backward-Facing Step," *Advances in Mechanical Engineering*, Vol. 5, 2013, pp. 147916.

[11]Jumper, E. and Fitzgerald, E., "Recent Advances in Aero-optics," *Progress in Aerospace Sciences*, Vol. 37, 2001, pp. 299–339.

[12]Guo, G., Tong, X., and Luo, Q., "Numerical Investigation on Image Degradation Caused by Aero-Optical Effects of the Supersonic Mixing Layer," *Applied Optics*, Vol. 59, No. 35, 2020.

[13]Yi, S., Tian, L., Zhao, Y., He, L., and Chen, Z., "Aero-Optic Aberration Measuring Method Based on NPLS and its Application," *Chinese Science Bulletin*, Vol. 55, No. 31, 2010, pp. 3545–3549.

[14]Zhi, C., Shihe, H., Yangzhu, Z., Yong, G., and Yu, W., "Spatial Density Fluctuation of Supersonic Flow over a Backward-Facing Step Measured by Nano-Tracer Planar Laser Scattering," *Journal of Vision*, Vol. 17, 2014, pp. 345–361.

[15]Ayyalasomayajula, H., Arunajatesan, S., C., K., and N., S., "Large Eddy Simulation of a Supersonic Flow Over a Backward-Facing Step For Aero-Optic Analysis," *AIAA Paper 2006-1416*, 2006.

[16]Gross, A. and Fasel, H., "High-Order WENO Schemes Based on the ROE Approximate Riemann Solver," *AIAA Paper 2002-2735*, 2002.

[17]Gross, A. and Fasel, H., "High-Order Accurate Numerical Method for Complex Flows," *AIAA Journal*, Vol. 46, No. 1, 2008, pp. 204–214.

[18]Balsara, D., Garain, S., and Shu, C. W., "An Efficient Class of WENO Schemes with Adaptive Order," *Journal of Computational Physics*, Vol. 326, 2016, pp. 780–804.

[19]Smits, A. J. and Dussauge, J.-P., *Turbulent shear layers in supersonic flow*, Springer Science & Business Media, 2006.

[20]Kawai, S. and Larsson, J., "Wall-Modeling in Large Eddy Simulation: Length scales, Grid Resolution, and Accuracy," *Physics of Fluids*, Vol. 24, 2012.

[21]Nicoud, F. and Ducros, F., "Subgrid-Scale Stress Modelling Based on the Square of the Velocity Gradient Tensor," *Flow, Turbulence and Combustion*, Vol. 62, No. 3, 1999, pp. 183–200.

[22]Stolz, S. and Adams, N., "Large-Eddy Simulation of High-Reynolds-Number Supersonic Boundary Layer using the Approximate Deconvolution Model and a Rescaling and Recycling Technique," *Physics of Fluids*, Vol. 15, No. 8, 2003, pp. 2398–2412.

[23]Gross, A., Castillo, P., and Lee, S., "Wall-Modeled Large-Eddy Simulations of Turbulent Shockwave Boundary Layer Interaction and Boundary Layer Flows," *AIAA Paper 2021-2749*, 2021.

[24]Gladstone, J. and Dale, T., "Researches on the Refraction, Dispersion, and Sensitivities of Liquids," *Philosophical Transactions of the Royal Society of London*, Vol. 153, 1863, pp. 317–343.

[25]Peck, E., , and Khanna, B., "Dispersion of Nitrogen," *Journal of the Optical Society of America*, Vol. 56, No. 8, 1966.

[26]Clergent, Y., Durou, C., and Laurens, M., "Refractive Index Variations for Argon, Nitrogen and Carbon Dioxide at $\lambda = 632.8$nm (He-Ne Laser Light) in the Range $288.15 \leq T \leq 323.15$ K, $0 < p < 110$ kPa," *Journal of Chemical & Engineering Data*, Vol. 44, 1999, pp. 197–199.

[27]Wang, K. and Wang, M., "Aero-Optics of Subsonic Turbulent Boundary Layers," *Journal of Fluid Mechanics*, Vol. 696, 2012, pp. 122–151.

[28]Lee, S. and Gross, A., "Large-Eddy Simulations of Supersonic Turbulent Boundary Layer," *AIAA Paper 2020-3076*, 2020.

[29]McDaniel, J., Fletcher, D., Hartfield, R., and Hollo, S., "Staged Transverse Injection into Mach 2 Flow Behind a Rearward-Facing-Step: A 3D Compressible Test Case for Hypersonic Combustor Code Validation," *AIAA Paper 1991-5071*, 1991.

[30]Bolgar, I., Scharnowski, S., and Kähler, C., "The Effect of the Mach Number on a Turbulent Backward-Facing Step Flow," *Flow, Turbulence and Combustion*, Vol. 101, No. 2, 2018, pp. 653–680.

[31]Riley, L., Ranjan, R., and Gaitonde, D., "Unsteadiness in a Supersonic Backward-Facing Step Flow," *AIAA Paper 2019-3343*, 2019.

[32]Soni, R. K., Arya, N., and De, A., "Characterization of Turbulent Supersonic Flow over a Backward-Facing Step," *AIAA Journal*, Vol. 55, No. 5, 2017, pp. 1511–1529.

[33]Jumper, E. and Gordeyev, S., "Physics and Measurement of Aero-Optical Effects: Past and Present," *Annual Review of Fluid Mechanics*, Vol. 49, No. 1, 2017, pp. 419–441.

[34]Gordeyev, S. and Juliano, T., "Optical Characterization of Nozzle-Wall Mach-6 Boundary Layers," *AIAA Paper 2016-1586*, 2016.

[35]Miller, N., Lynch, K., Gordeyev, S., Guildenbecher, R., Duan, L., and Wagnild, R., "Aero-optical Distortions of Turbulent Boundary Layers: Hypersonic DNS," *AIAA Paper 2022-0056*, 2022.

[36]Castillo, P., Gross, A., Miller, N., Guildenbecher, D., and Lynch, K., "Wall-Modeled Large-Eddy Simulations of Turbulent Mach 3.5, 8, and 14 Boundary Layers - Effect of Mach Number on Aero-Optical Distortions," *AIAA Paper 2022-3441*, 2022.

[37]Lynch, K., Spillers, R., Miller, N., Guildenbecher, D., and Gordeyev, S., "Aero-Optical Measurements of a Mach 8 Boundary Layer," *AIAA Paper 2021-2831*, 2021.

[38]Lynch, K., Miller, N., Guildenbecher, D., Butler, L., and Gordeyev, S., "Aero-Optical Measurements of a Mach 8 Boundary Layer," *AIAA Journal*, Vol. 61, No. 3, 2023, pp. 991–1001.